

A finite-volume method based on compact local integrated radial basis function approximations for second-order differential problems

T.-T. Hoang-Trieu¹, N. Mai-Duy¹, C.-D. Tran¹ and T. Tran-Cong¹

Abstract: In this paper, compact local integrated radial basis function (IRBF) stencils reported in [Mai-Duy and Tran-Cong (2011) *Journal of Computational Physics* 230(12), 4772-4794] are introduced into the finite-volume / subregion - collocation formulation for the discretisation of second-order differential problems defined on rectangular and non-rectangular domains. The problem domain is simply represented by a Cartesian grid, over which overlapping compact local IRBF stencils are utilised to approximate the field variable and its derivatives. The governing differential equation is integrated over non-overlapping control volumes associated with grid nodes, and the divergence theorem is then applied to convert volume integrals into surface/line integrals. Line integrals are evaluated by means of the middle point rule (i.e. second-order integration scheme) and three-point Gaussian quadrature rule (i.e. high-order integration scheme). The accuracy of the proposed method is numerically investigated through the solution of several test problems including natural convection in an annulus. Numerical results indicate that (i) the proposed method produces accurate results using relatively coarse grids and (ii) the three-point integration scheme is generally more accurate than the middle point scheme.

Keywords: Integrated radial basis functions, Compact local stencils, High-order approximations, Finite volume method, Natural convection.

1 Introduction

Radial basis functions (RBFs) are known as a powerful high-order approximation tool for scattered data [Kansa (1990a); Haykin (1999)]. The application of RBFs for the solution of partial differential equations (PDEs) has received a great deal of attention over the last twenty years [Fasshauer (2007)]. One can construct the

¹ Computational Engineering and Science Research Centre, Faculty of Engineering and Surveying, University of Southern Queensland, Toowoomba, QLD 4350, Australia.

RBF approximations through differentiation (DRBFs) [Kansa (1990b); Zerroukat, Power, and Chen (1998); Fornberg and Flyer (2005)] or integration (IRBFs) [Mai-Duy and Tran-Cong (2001a,b)]. For the former, a function is decomposed into a set of RBFs. For the latter, RBFs are employed to represent highest-order derivatives under consideration and then integrated to yield approximate expressions for lower-order derivatives and the function itself. IRBFs have the ability to avoid the reduction of convergence rate caused by differentiation and also to improve the numerical stability of a discrete solution. In recent years, research effort has been focused on constructing the RBF approximations in local form (to obtain sparse system matrices) [Shu, Ding, and Yeo (2003); Lee, Liu, and Fan (2003); Sarler (2005); Mai-Duy and Tran-Cong (2009)] and in compact local form (to obtain both sparse system matrices and high rates of convergence of the approximate solution) [Tolstykh and Shirobokov (2005); Wright and Fornberg (2006); Mai-Duy and Tran-Cong (2011); Thai-Quang, Le-Cao, Mai-Duy, and Tran-Cong (2012); Hoang-Trieu, Mai-Duy, and Tran-Cong (2012)]. It is known that the width of RBFs (shape parameter) strongly affects the quality of the approximations [Kansa (1990a); Rippa (1999); Fornberg and Wright (2004); Larsson and Fornberg (2005)]. In local forms, RBFs can work with a wide range of the RBF width and their solution accuracy can thus be effectively controlled by means of the spatial discretisation size and/or the RBF width.

Finite volume methods (FVMs), which conserve mass, momentum and energy over any control volume and can work effectively with complex geometry problems, are widely used in computational fluid dynamic (CFD) [Patankar (1980); Eymard, Gallouet, and Herbin (2000); Huilgol and Phan-Thien (1997); Pereira, Kobayashi, and Pereira (2001)]. It should be pointed out that the accuracy of a finite-volume solution is decided not only by the way to approximate the field variable but also by numerical integration schemes used for evaluating line/surface integrals in the formulation. Epperson (2002) has shown that, given exact nodal function values, using a n -point Gaussian quadrature rule can lead to a solution whose error is $O(h^{2n})$, where h is the discretisation size. As a result, the error is of order up to h^2 only if one uses the middle point rule (i.e. one point Gaussian quadrature rule). Moroney and Turner (2006) proposed a FVM method, where differentiated RBFs are employed as a means of local gradient interpolation and the underlying line integrals are evaluated using the three-point Gaussian quadrature rule. Numerical results showed that the method yields accuracy several orders of magnitude better than simpler methods based on shape functions for both linear and nonlinear diffusion problems.

In this paper, compact local integrated RBF stencils [Mai-Duy and Tran-Cong (2011)] are incorporated into the FV formulation to discretise second-order differ-

ential equations in one (1D) and two (2D) dimensions. Two numerical integration schemes, namely the middle point rule and 3-point Gaussian quadrature rule, are employed and their effects on the solution accuracy are investigated. We also study the accuracy behaviour against the RBF width. Results obtained are compared with standard FVMs as well as point collocation methods employed with compact local IRBF stencils. The remainder of this paper is organised as follows. A brief review of integrated RBFs including compact local approximations is given in Section 2. The proposed method is described for 1D and 2D problems in Section 3 and then verified in Section 4. Section 5 concludes the papers.

2 Brief review of integrated RBFs

Consider a function $u(\mathbf{x})$. The integral formulation starts with the decomposition of highest-order derivatives under consideration into a set of RBFs. For second-order differential problems, one has

$$\frac{\partial^2 u(\mathbf{x})}{\partial \eta^2} = \sum_{i=1}^n w_i I_i^{(2)}(\mathbf{x}), \quad \mathbf{x} \in \Omega, \tag{1}$$

where η is used to denote a component of the position vector \mathbf{x} (e.g. η can be x for 1D problems, and x or y for 2D problems); Ω is the domain of interest; $\{w_i\}_{i=1}^n$ is the set of unknown RBF coefficients; and $\{I_{i[\eta]}^{(2)}(\mathbf{x})\}_{i=1}^n$ is the set of RBFs. We will implement (1) with the multiquadric RBF (MQ)

$$I_i^{(2)}(\mathbf{x}) = \sqrt{(\mathbf{x} - c_i)^2 + a_i^2}, \tag{2}$$

where c_i and a_i are the centre and the width of the i th MQ, respectively.

Approximate expressions for first-order derivatives and the function u itself are then obtained by integrating expression (1)

$$\frac{\partial u(\mathbf{x})}{\partial \eta} = \sum_{i=1}^n w_i I_i^{(1)}(\mathbf{x}) + C_1^{[\eta]}, \tag{3}$$

$$u(\mathbf{x}) = \sum_{i=1}^n w_i I_i^{(0)}(\mathbf{x}) + \eta C_1^{[\eta]} + C_2^{[\eta]}, \tag{4}$$

where $I_i^{(1)}(\mathbf{x}) = \int I_i^{(2)}(\mathbf{x}) d\eta$; $I_i^{(0)}(\mathbf{x}) = \int I_i^{(1)}(\mathbf{x}) d\eta$; and $C_1^{[\eta]}$ and $C_2^{[\eta]}$ are the ‘‘constants’’ of integration. $C_1^{[\eta]}$ and $C_2^{[\eta]}$ will be constants for 1D problems, functions in one variable for 2D problems, and in two variables for 3D problems. These functions are unknown and can be approximated as linear combinations of basis functions.

The approximations (1)-(4) are called a global IRBF scheme if one employs these expressions over the entire domain, a 1D-IRBF scheme if they are employed along grid lines, and a local IRBF scheme if they are employed over small overlapping subregions. Global schemes can yield a high rate of convergence, but their matrices are fully populated and thus very costly for solving large-scale problems. On the other hand, local schemes result in sparse matrices that can be handled in a very efficient way, but their accuracies are deteriorated significantly. Several treatments were proposed to improve the solution accuracy of local IRBF schemes. One simple but effective way is to incorporate, through the constants of integration, nodal values of the governing equation or of first/second derivatives into the local approximations. Such approximations are called a compact local IRBF scheme. It was shown numerically that compact local IRBF schemes are superior to local IRBF ones regarding both the computational cost and the accuracy in the context of point-collocation formulation. In the present work, compact local IRBF stencils are introduced into the subregion-collocation/finite-volume formulation for the solution of second-order differential problems defined on rectangular and non-rectangular domains.

3 Proposed method

The proposed finite-volume method, which is based on compact local IRBF stencils, (CLIRBF-FVM) is first described for 1D problems and then extended to 2D problems.

3.1 One dimensional problems

Consider a 1D problem governed by

$$\frac{d^2u(x)}{dx^2} + \frac{du(x)}{dx} + u(x) = f(x), \quad x \in \Omega, \quad (5)$$

where $u(x)$ and $f(x)$ are continuous and prescribed functions, respectively. The domain Ω is subdivided into a set of non-overlapping line segments (control volumes) that are associated with grid nodes. Figure 1 shows a full control volume for an interior grid node x_i , ($i \in \{2, 3, \dots, n-1\}$) and a half control volume for a boundary node x_i ($i \in \{1, n\}$). Integrating (5) over the full control volume Ω_i results in

$$\int_{\Omega_i} \left(\frac{d^2u(x)}{dx^2} + \frac{du(x)}{dx} + u(x) \right) d\Omega_i = \int_{\Omega_i} f(x) d\Omega_i, \quad (6)$$

or

$$\frac{du(x_{i+1/2})}{dx} - \frac{du(x_{i-1/2})}{dx} + u(x_{i+1/2}) - u(x_{i-1/2}) + \int_{x_{i-1/2}}^{x_{i+1/2}} u(x)dx = \int_{x_{i-1/2}}^{x_{i+1/2}} f(x)dx. \quad (7)$$

The integrals on the left and right sides of equation (7) are evaluated using the middle point rule and also the three point Gaussian quadrature rule.

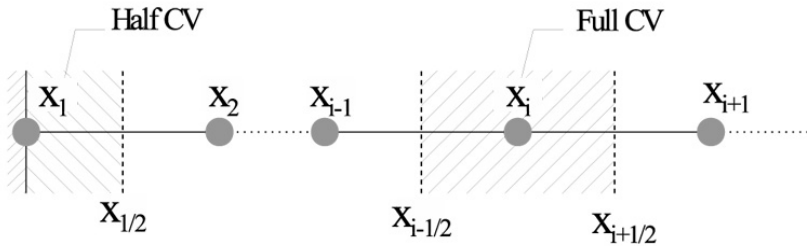


Figure 1: A schematic diagram for the CV formulation in 1D.

For the former, the integrals are expressed as

$$\int_{x_{i-1/2}}^{x_{i+1/2}} u(x)dx = u(x_i)\Delta x, \quad (8)$$

$$\int_{x_{i-1/2}}^{x_{i+1/2}} f(x)dx = f(x_i)\Delta x, \quad (9)$$

where $\Delta x = x_{i+1/2} - x_{i-1/2}$.

For the latter, the integrals are expressed as

$$\int_{x_{i-1/2}}^{x_{i+1/2}} u(x)dx = \frac{\Delta x}{2} \sum_{k=1}^3 \gamma_k u\left(\frac{x_{i+1/2} - x_{i-1/2}}{2} \zeta_k + \frac{x_{i+1/2} + x_{i-1/2}}{2}\right), \quad (10)$$

$$\int_{x_{i-1/2}}^{x_{i+1/2}} f(x)dx = \frac{\Delta x}{2} \sum_{k=1}^3 \gamma_k f\left(\frac{x_{i+1/2} - x_{i-1/2}}{2} \zeta_k + \frac{x_{i+1/2} + x_{i-1/2}}{2}\right), \quad (11)$$

$$\{\gamma_k\}_{k=1}^3 = \left\{ \frac{5}{9}, \frac{8}{9}, \frac{5}{9} \right\}, \quad \{\zeta_k\}_{k=1}^3 = \left\{ -\sqrt{\frac{3}{5}}, 0, +\sqrt{\frac{3}{5}} \right\}, \quad (12)$$

where γ_k and ζ_k are the weights and Gauss points, respectively.

We now approximate the field variable u and its derivatives in equations (7), (8) - (11) using compact local IRBFs. Over a 3-node stencil $[x_{i-1}, x_i, x_{i+1}]$ associated with grid node x_i , the relation between the physical space and the RBF weight space can be established as

$$\begin{pmatrix} u_{i-1} \\ u_i \\ u_{i+1} \\ f_{i-1} \\ f_{i+1} \end{pmatrix} = \underbrace{\begin{bmatrix} \mathcal{H}^{(0)} \\ \mathcal{H} \end{bmatrix}}_{\mathcal{C}} \begin{pmatrix} w_1 \\ w_2 \\ w_3 \\ c_1 \\ c_2 \end{pmatrix}, \tag{13}$$

where nodal values of the governing equation at grid nodes x_{i-1} and x_{i+1} (i.e. f_{i-1} and f_{i+1}) are also included, \mathcal{C} is the conversion matrix, and $\mathcal{H}^{(0)}$ and \mathcal{H} are submatrices defined as

$$\mathcal{H}^{(0)} = \begin{bmatrix} I_1^{(0)}(x_{i-1}), & I_2^{(0)}(x_{i-1}), & I_3^{(0)}(x_{i-1}), & x_{i-1}, & 1 \\ I_1^{(0)}(x_i), & I_2^{(0)}(x_i), & I_3^{(0)}(x_i), & x_i, & 1 \\ I_1^{(0)}(x_{i+1}), & I_2^{(0)}(x_{i+1}), & I_3^{(0)}(x_{i+1}), & x_{i+1}, & 1 \end{bmatrix},$$

$$\mathcal{H} = \begin{bmatrix} \mathcal{G}_1(x_{i-1}), & \mathcal{G}_2(x_{i-1}), & \mathcal{G}_3(x_{i-1}), & x_{i-1} + 1, & 1 \\ \mathcal{G}_1(x_{i+1}), & \mathcal{G}_2(x_{i+1}), & \mathcal{G}_3(x_{i+1}), & x_{i+1} + 1, & 1 \end{bmatrix},$$

in which $\mathcal{G}_k(x) = I_k^{(2)}(x) + I_k^{(1)}(x) + I_k^{(0)}(x)$ with $k \in \{1, 2, 3\}$. It is noted that the subscripts $i - 1, i$ and $i + 1$ are used to represent the nodes of the stencil in a global definition, while 1, 2 and 3 denote the nodes of the stencil in a local definition.

Solving (13) yields

$$\begin{pmatrix} w_1 \\ w_2 \\ w_3 \\ c_1 \\ c_2 \end{pmatrix} = \mathcal{C}^{-1} \begin{pmatrix} u_{i-1} \\ u_i \\ u_{i+1} \\ f_{i-1} \\ f_{i+1} \end{pmatrix}. \tag{14}$$

Values of the field variable and its derivatives at an arbitrary point on the stencil can thus be calculated in the physical space as

$$u(x) = \left[I_1^{(0)}(x), I_2^{(0)}(x), I_3^{(0)}(x), x, 1 \right] \mathcal{C}^{-1} \begin{pmatrix} \hat{u} \\ \hat{f} \end{pmatrix}, \tag{15}$$

$$\frac{du(x)}{dx} = \left[I_1^{(1)}(x), I_2^{(1)}(x), I_3^{(1)}(x), 1, 0 \right] \mathcal{C}^{-1} \begin{pmatrix} \hat{u} \\ \hat{f} \end{pmatrix}, \tag{16}$$

$$\frac{d^2u(x)}{dx^2} = \left[I_1^{(2)}(x), I_2^{(2)}(x), I_3^{(2)}(x), 0, 0 \right] \mathcal{C}^{-1} \begin{pmatrix} \hat{u} \\ \hat{f} \end{pmatrix}, \tag{17}$$

where $x_{i-1} < x < x_{i+1}$, $\hat{u} = (u_{i-1}, u_i, u_{i+1})^T$, and $\hat{f} = (f_{i-1}, f_{i+1})^T$.

We consider two types of boundary conditions

(i) *Dirichlet boundary conditions*: Since values of u are given at x_1 and x_n , the discretisation is carried out for full control volumes only.

(ii) *Dirichlet and Neumann boundary conditions*: Since the first derivative du/dx instead of the field variable u is given at a boundary node, one needs to generate one additional algebraic equation for the value of u at that node. This can be achieved by conducting the discretisation over a half control volume associated with the boundary node.

3.2 Two dimensional problems

3.2.1 Poisson equation

The governing equation here takes the form

$$\nabla^2 u(\mathbf{x}) = f(\mathbf{x}), \quad \mathbf{x} \in \Omega. \tag{18}$$

Rectangular domains:

We discretise the problem domain using a Cartesian grid of density $n_x \times n_y$. Control volumes associated with grid nodes are of rectangular shapes that do not overlap each other. Consider an interior node $\mathbf{x}_{i,j}$ ($2 \leq i \leq n_x - 1; 2 \leq j \leq n_y - 1$). Its associated 9-node stencil is defined globally as

$$\begin{bmatrix} \mathbf{x}_{i-1,j+1} & \mathbf{x}_{i,j+1} & \mathbf{x}_{i+1,j+1} \\ \mathbf{x}_{i-1,j} & \mathbf{x}_{i,j} & \mathbf{x}_{i+1,j} \\ \mathbf{x}_{i-1,j-1} & \mathbf{x}_{i,j-1} & \mathbf{x}_{i+1,j-1} \end{bmatrix},$$

and locally as

$$\begin{bmatrix} \mathbf{x}_3 & \mathbf{x}_6 & \mathbf{x}_9 \\ \mathbf{x}_2 & \mathbf{x}_5 & \mathbf{x}_8 \\ \mathbf{x}_1 & \mathbf{x}_4 & \mathbf{x}_7 \end{bmatrix},$$

where the grid nodes are numbered from bottom to top and from left to right. Figure 2 shows a schematic diagram for a full control volume associated with an interior node and a half control volume associated with a boundary node.

Integrating (18) over a full control volume Ω_s yields

$$\int_{\Omega_s} \nabla^2 u(\mathbf{x}) d\Omega_s = \int_{\Omega_s} f(\mathbf{x}) d\Omega_s. \tag{19}$$

By means of the divergence theorem, (19) reduces to

$$\oint_{\Gamma_s} \nabla u(\mathbf{x}) \cdot \hat{n} d\Gamma_s = \int_{\Omega_s} f(\mathbf{x}) d\Omega_s, \tag{20}$$

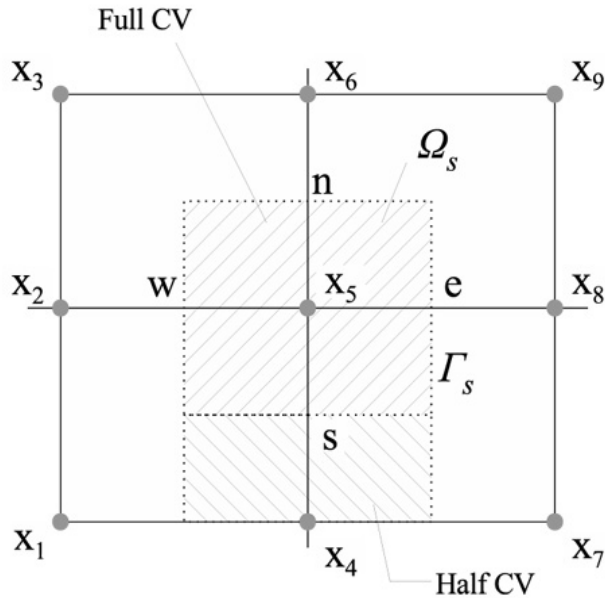


Figure 2: A schematic diagram for the CV formulation in 2D.

or

$$\int_{y_s}^{y_n} \frac{\partial u(\mathbf{x})}{\partial x} \Big|_e dy - \int_{y_s}^{y_n} \frac{\partial u(\mathbf{x})}{\partial x} \Big|_w dy + \int_{x_w}^{x_e} \frac{\partial u(\mathbf{x})}{\partial y} \Big|_n dx - \int_{x_w}^{x_e} \frac{\partial u(\mathbf{x})}{\partial y} \Big|_s dx = \int_{\Omega_s} f(\mathbf{x}) d\Omega_s, \quad (21)$$

where Γ_s is the interface of the control volume, \hat{n} is the outward unit normal vector, and $|_e$, $|_w$, $|_n$ and $|_s$ denote the east, west, north and south faces of the control volume, respectively.

If the middle point rule is applied to (20), one obtains

$$\left(\frac{\partial u(\mathbf{x}_e)}{\partial x} - \frac{\partial u(\mathbf{x}_w)}{\partial x} \right) \Delta y + \left(\frac{\partial u(\mathbf{x}_n)}{\partial y} - \frac{\partial u(\mathbf{x}_s)}{\partial y} \right) \Delta x = \Delta x \Delta y f(\mathbf{x}), \quad (22)$$

where the subscripts e, w, n and s are used to indicate the intersections of the grid lines with the east, west, north and south faces of the control volume, respectively; $\Delta x = x_e - x_w$ and $\Delta y = y_n - y_s$.

If the three-point Gaussian quadrature rule is applied to (20), one obtains

$$\begin{aligned} \frac{\Delta y}{2} \sum_{j=1}^3 \gamma_j \frac{\partial u(y(\zeta_j))}{dx} \Big|_e - \frac{\Delta y}{2} \sum_{j=1}^3 \gamma_j \frac{\partial u(y(\zeta_j))}{dx} \Big|_w + \frac{\Delta x}{2} \sum_{i=1}^3 \gamma_i \frac{\partial u(x(\zeta_i))}{dy} \Big|_n \\ - \frac{\Delta x}{2} \sum_{i=1}^3 \gamma_i \frac{\partial u(x(\zeta_i))}{dy} \Big|_s = \frac{\Delta x \Delta y}{4} \sum_{i=1}^3 \sum_{j=1}^3 \gamma_i \gamma_j f(x(\zeta_i), y(\zeta_j)), \end{aligned} \tag{23}$$

where γ_i and ζ_i are defined as before.

Now we approximate gradients in (22) and (23) using compact local IRBF approximations defined over overlapping 3×3 stencils. The conversion matrix for each stencil is constructed as

$$\begin{pmatrix} \widehat{u} \\ \widehat{0} \\ \widehat{f} \end{pmatrix} = \underbrace{\begin{bmatrix} \mathcal{H}_x^{(0)}, & \mathcal{O} \\ \mathcal{H}_x^{(0)}, & -\mathcal{H}_y^{(0)} \\ \mathcal{H}_x, & \mathcal{H}_y \end{bmatrix}}_{\mathcal{C}} \begin{pmatrix} \widehat{w}_x \\ \widehat{w}_y \end{pmatrix} \tag{24}$$

where $\widehat{0}$ and \mathcal{O} are a zero vector and zero matrix, respectively; \widehat{u} and $\widehat{0}$ are vectors of length 9; \widehat{w}_x and \widehat{w}_y are the RBF coefficient vectors of length 15; \mathcal{O} , $\mathcal{H}_x^{(0)}$, $\mathcal{H}_y^{(0)}$ are matrices of dimensions 9×15 , and \mathcal{H}_x and \mathcal{H}_y are matrices of dimensions 4×15 . Equations $\widehat{u} = \mathcal{H}_x^{(0)} \widehat{w}_x$ are employed to collocate the variable u over the stencil; equations $\mathcal{H}_x^{(0)} \widehat{w}_x - \mathcal{H}_y^{(0)} \widehat{w}_y = \widehat{0}$ are employed to enforce nodal values of u obtained from the integration with respect to x and y to be identical; equations $\mathcal{H}_x \widehat{w}_x + \mathcal{H}_y \widehat{w}_y = \widehat{f}$ are employed to represent values of the PDE (18) at selected nodes;

$$\begin{aligned} \widehat{u} &= (u_1, \dots, u_9)^T, \\ \widehat{w}_x &= \left(w_1^{[x]}, \dots, w_9^{[x]}, c_1^{[x]}(y_1), c_1^{[x]}(y_2), c_1^{[x]}(y_3), c_2^{[x]}(y_1), c_2^{[x]}(y_2), c_2^{[x]}(y_3) \right)^T, \\ \widehat{w}_y &= \left(w_1^{[y]}, \dots, w_9^{[y]}, c_1^{[y]}(x_1), c_1^{[y]}(x_4), c_1^{[y]}(x_7), c_2^{[y]}(x_1), c_2^{[y]}(x_4), c_2^{[y]}(x_7) \right)^T, \end{aligned}$$

$$\mathcal{H}_x^{(0)} = \begin{bmatrix} I_{[x]1}^{(0)}(\mathbf{x}_1), & \cdots, & I_{[x]9}^{(0)}(\mathbf{x}_1), & x_1, & 0, & 0, & 1, & 0, & 0 \\ I_{[x]1}^{(0)}(\mathbf{x}_2), & \cdots, & I_{[x]9}^{(0)}(\mathbf{x}_2), & 0, & x_2, & 0, & 0, & 1, & 0 \\ I_{[x]1}^{(0)}(\mathbf{x}_3), & \cdots, & I_{[x]9}^{(0)}(\mathbf{x}_3), & 0, & 0, & x_3, & 0, & 0, & 1 \\ I_{[x]1}^{(0)}(\mathbf{x}_4), & \cdots, & I_{[x]9}^{(0)}(\mathbf{x}_4), & x_1, & 0, & 0, & 1, & 0, & 0 \\ I_{[x]1}^{(0)}(\mathbf{x}_5), & \cdots, & I_{[x]9}^{(0)}(\mathbf{x}_5), & 0, & x_2, & 0, & 0, & 1, & 0 \\ I_{[x]1}^{(0)}(\mathbf{x}_6), & \cdots, & I_{[x]9}^{(0)}(\mathbf{x}_6), & 0, & 0, & x_3, & 0, & 0, & 1 \\ I_{[x]1}^{(0)}(\mathbf{x}_7), & \cdots, & I_{[x]9}^{(0)}(\mathbf{x}_7), & x_1, & 0, & 0, & 1, & 0, & 0 \\ I_{[x]1}^{(0)}(\mathbf{x}_8), & \cdots, & I_{[x]9}^{(0)}(\mathbf{x}_8), & 0, & x_2, & 0, & 0, & 1, & 0 \\ I_{[x]1}^{(0)}(\mathbf{x}_9), & \cdots, & I_{[x]9}^{(0)}(\mathbf{x}_9), & 0, & 0, & x_3, & 0, & 0, & 1 \end{bmatrix},$$

$$\mathcal{H}_y^{(0)} = \begin{bmatrix} I_{[y]1}^{(0)}(\mathbf{x}_1), & \cdots, & I_{[y]9}^{(0)}(\mathbf{x}_1), & y_1, & 0, & 0, & 1, & 0, & 0 \\ I_{[y]1}^{(0)}(\mathbf{x}_2), & \cdots, & I_{[y]9}^{(0)}(\mathbf{x}_2), & y_2, & 0, & 0, & 1, & 0, & 0 \\ I_{[y]1}^{(0)}(\mathbf{x}_3), & \cdots, & I_{[y]9}^{(0)}(\mathbf{x}_3), & y_3, & 0, & 0, & 1, & 0, & 0 \\ I_{[y]1}^{(0)}(\mathbf{x}_4), & \cdots, & I_{[y]9}^{(0)}(\mathbf{x}_4), & 0, & y_4, & 0, & 0, & 1, & 0 \\ I_{[y]1}^{(0)}(\mathbf{x}_5), & \cdots, & I_{[y]9}^{(0)}(\mathbf{x}_5), & 0, & y_5, & 0, & 0, & 1, & 0 \\ I_{[y]1}^{(0)}(\mathbf{x}_6), & \cdots, & I_{[y]9}^{(0)}(\mathbf{x}_6), & 0, & y_6, & 0, & 0, & 1, & 0 \\ I_{[y]1}^{(0)}(\mathbf{x}_7), & \cdots, & I_{[y]9}^{(0)}(\mathbf{x}_7), & 0, & 0, & y_7, & 0, & 0, & 1 \\ I_{[y]1}^{(0)}(\mathbf{x}_8), & \cdots, & I_{[y]9}^{(0)}(\mathbf{x}_8), & 0, & 0, & y_8, & 0, & 0, & 1 \\ I_{[y]1}^{(0)}(\mathbf{x}_9), & \cdots, & I_{[y]9}^{(0)}(\mathbf{x}_9), & 0, & 0, & y_9, & 0, & 0, & 1 \end{bmatrix}.$$

In this study, selected nodes for $\mathcal{H}_x \widehat{w}_x + \mathcal{H}_y \widehat{w}_y = \widehat{f}$ are chosen as $(\mathbf{x}_2, \mathbf{x}_4, \mathbf{x}_6, \mathbf{x}_8)$ so that

$$\mathcal{H}_x = \begin{bmatrix} I_{[x]1}^{(2)}(\mathbf{x}_2), & \cdots, & I_{[x]9}^{(2)}(\mathbf{x}_2), & 0, & 0, & 0, & 0, & 0, & 0 \\ I_{[x]1}^{(2)}(\mathbf{x}_4), & \cdots, & I_{[x]9}^{(2)}(\mathbf{x}_4), & 0, & 0, & 0, & 0, & 0, & 0 \\ I_{[x]1}^{(2)}(\mathbf{x}_6), & \cdots, & I_{[x]9}^{(2)}(\mathbf{x}_6), & 0, & 0, & 0, & 0, & 0, & 0 \\ I_{[x]1}^{(2)}(\mathbf{x}_8), & \cdots, & I_{[x]9}^{(2)}(\mathbf{x}_8), & 0, & 0, & 0, & 0, & 0, & 0 \end{bmatrix},$$

$$\mathcal{H}_y = \begin{bmatrix} I_{[y]1}^{(2)}(\mathbf{x}_2), & \cdots, & I_{[y]9}^{(2)}(\mathbf{x}_2), & 0, & 0, & 0, & 0, & 0, & 0 \\ I_{[y]1}^{(2)}(\mathbf{x}_4), & \cdots, & I_{[y]9}^{(2)}(\mathbf{x}_4), & 0, & 0, & 0, & 0, & 0, & 0 \\ I_{[y]1}^{(2)}(\mathbf{x}_6), & \cdots, & I_{[y]9}^{(2)}(\mathbf{x}_6), & 0, & 0, & 0, & 0, & 0, & 0 \\ I_{[y]1}^{(2)}(\mathbf{x}_8), & \cdots, & I_{[y]9}^{(2)}(\mathbf{x}_8), & 0, & 0, & 0, & 0, & 0, & 0 \end{bmatrix}.$$

Solving (24) yields

$$\begin{pmatrix} \widehat{w}_x \\ \widehat{w}_y \end{pmatrix} = \mathcal{C}^{-1} (\widehat{u}, \widehat{0}, \widehat{f})^T, \tag{25}$$

or $\widehat{w}_x = \mathcal{C}_x^{-1}(\widehat{u}, \widehat{0}, \widehat{f})^T$ and $\widehat{w}_y = \mathcal{C}_y^{-1}(\widehat{u}, \widehat{0}, \widehat{f})^T$, where \mathcal{C}_x^{-1} and \mathcal{C}_y^{-1} are the first and the last 15 rows of matrix \mathcal{C}^{-1} . Substitution of \widehat{w}_x and \widehat{w}_y into (3) defined over the stencil leads to

$$\frac{\partial u(\mathbf{x})}{\partial x} = \mathcal{H}_x^{(1)}(\mathbf{x}) \mathcal{C}_x^{-1}(\widehat{u}, \widehat{0}, \widehat{f})^T, \tag{26}$$

$$\frac{\partial u(\mathbf{x})}{\partial y} = \mathcal{H}_y^{(1)}(\mathbf{x}) \mathcal{C}_y^{-1}(\widehat{u}, \widehat{0}, \widehat{f})^T, \tag{27}$$

where

$$\mathcal{H}_x^{(1)}(\mathbf{x}) = [I_{[x]1}^{(1)}(\mathbf{x}), \dots, I_{[x]9}^{(1)}(\mathbf{x}), J_{[y]1}(y), J_{[y]2}(y), J_{[y]3}(y), 0, 0, 0], \tag{28}$$

$$\mathcal{H}_y^{(1)}(\mathbf{x}) = [I_{[y]1}^{(1)}(\mathbf{x}), \dots, I_{[y]9}^{(1)}(\mathbf{x}), J_{[x]1}(x), J_{[x]2}(x), J_{[x]3}(x), 0, 0, 0], \tag{29}$$

in which $\{J_{[y]1}(y), J_{[y]2}(y), J_{[y]3}(y)\}$ and $\{J_{[x]1}(x), J_{[x]2}(x), J_{[x]3}(x)\}$ are sets of basis functions used for the approximation of integration ‘‘constants’’ $C_1^{[x]}(y)$ and $C_1^{[y]}(x)$ in equations (3)-(4), respectively

$$C_1^{[x]}(y) = c_1^{[x]}(y_1)J_{[y]1}(y) + c_1^{[x]}(y_2)J_{[y]2}(y) + c_1^{[x]}(y_3)J_{[y]3}(y), \tag{30}$$

$$C_1^{[y]}(x) = c_1^{[y]}(x_1)J_{[x]1}(x) + c_1^{[y]}(x_4)J_{[x]2}(x) + c_1^{[y]}(x_7)J_{[x]3}(x). \tag{31}$$

In a similar way, values of the field variable and its second derivatives are obtained by substituting \widehat{w}_x and \widehat{w}_y into (4) and (1), respectively.

It can be seen that the approximations for u and its derivatives are expressed in terms of nodal values of the field variable and of the governing equation. For Dirichlet boundary conditions only, the discretisation is carried out over full control volumes associated with interior grid nodes. For Neumann boundary conditions, extra equations are needed and they are generated from half control volumes associated with the boundary nodes.

Non-rectangular domains:

We embed the problem domain in a rectangular domain and then discretise it using a Cartesian grid of density $n_x \times n_y$. Only Dirichlet boundary conditions are considered here. There are three types of nodes, namely (i) the boundary nodes (the intersections of the grid lines and the boundary); (ii) normal interior nodes, where their associated stencils lie within the problem domain entirely; and (iii) special

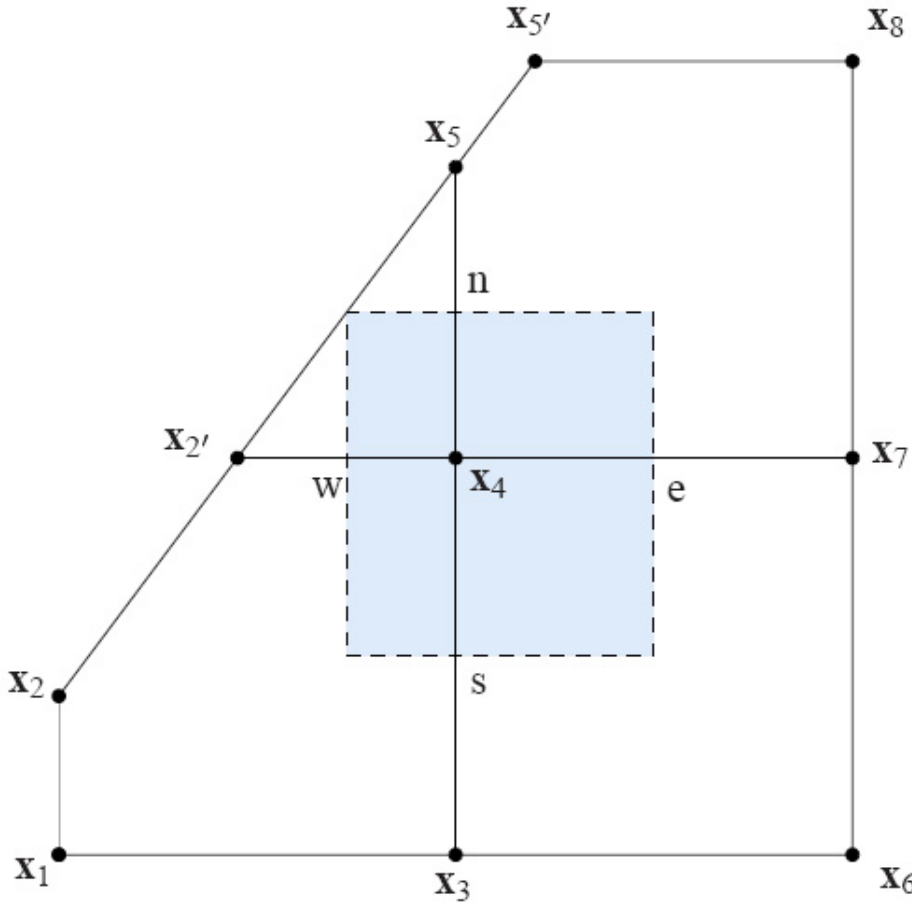


Figure 3: A schematic diagram for the CV formulation in 2D, where the stencil is cut by the boundary.

interior nodes, where their associated stencils are cut by the boundary. For the third type, which is typically illustrated in Figure 3, some special treatments are required. We employ nodes $[x_1, x_2', x_3, x_4, x_5', x_6, x_7, x_8]$ for the IRBF approximations with respect to the x direction, and $[x_1, x_2, x_3, x_4, x_5, x_6, x_7, x_8]$ for the y direction. Furthermore, in the conversion process (24), the governing equation is collocated at regular grid nodes only (e.g. x_3 and x_7). Note that the intersections of the x and y grid lines are considered as regular nodes, while the intersections of the grid lines and the non-rectangular boundaries are considered as irregular nodes. The remaining tasks here are similar to those of the rectangular-domain case.

3.2.2 Natural convection flow

The dimensionless governing equations for natural convection flow can be written in terms of the streamfunction ψ , vorticity ω , and temperature T as

$$\frac{\partial T}{\partial t} + \sqrt{RaPr} \left(\frac{\partial(uT)}{\partial x} + \frac{\partial(vT)}{\partial y} \right) = \frac{\partial^2 T}{\partial x^2} + \frac{\partial^2 T}{\partial y^2}, \quad (32)$$

$$-\omega = \frac{\partial^2 \psi}{\partial x^2} + \frac{\partial^2 \psi}{\partial y^2}, \quad (33)$$

$$\frac{\partial \omega}{\partial t} + \sqrt{\frac{Ra}{Pr}} \left(\frac{\partial(u\omega)}{\partial x} + \frac{\partial(v\omega)}{\partial y} - \frac{\partial T}{\partial x} \right) = \frac{\partial^2 \omega}{\partial x^2} + \frac{\partial^2 \omega}{\partial y^2}, \quad (34)$$

where $u = \frac{\partial \psi}{\partial y}$ and $v = -\frac{\partial \psi}{\partial x}$, Ra is the Rayleigh number, and Pr is the Prandtl number. Integrating (32)-(34) over a control volume Ω_s results in

$$\begin{aligned} \frac{\partial}{\partial t} \int_{\Omega_s} T d\Omega_s + \sqrt{RaPr} \int_{\Omega_s} \left(\frac{\partial(uT)}{\partial x} + \frac{\partial(vT)}{\partial y} \right) d\Omega_s = \\ \int_{\Omega_s} \left(\frac{\partial^2 T}{\partial x^2} + \frac{\partial^2 T}{\partial y^2} \right) d\Omega_s, \end{aligned} \quad (35)$$

$$-\int_{\Omega_s} \omega d\Omega_s = \int_{\Omega_s} \left(\frac{\partial^2 \psi}{\partial x^2} + \frac{\partial^2 \psi}{\partial y^2} \right) d\Omega_s, \quad (36)$$

$$\begin{aligned} \frac{\partial}{\partial t} \int_{\Omega_s} \omega d\Omega_s + \sqrt{\frac{Ra}{Pr}} \int_{\Omega_s} \left(\frac{\partial(u\omega)}{\partial x} + \frac{\partial(v\omega)}{\partial y} - \frac{\partial T}{\partial x} \right) d\Omega_s = \\ \int_{\Omega_s} \left(\frac{\partial^2 \omega}{\partial x^2} + \frac{\partial^2 \omega}{\partial y^2} \right) d\Omega_s. \end{aligned} \quad (37)$$

Assume that T and ω are linear over the time interval $(t^{(k-1)}, t^{(k)})$, the time derivative terms in (35) and (37) reduce to

$$\frac{\partial}{\partial t} \int_{\Omega_s} T d\Omega_s = \frac{\int_{\Omega_s} T^{(k)} d\Omega_s - \int_{\Omega_s} T^{(k-1)} d\Omega_s}{\Delta t}, \quad (38)$$

$$\frac{\partial}{\partial t} \int_{\Omega_s} \omega d\Omega_s = \frac{\int_{\Omega_s} \omega^{(k)} d\Omega_s - \int_{\Omega_s} \omega^{(k-1)} d\Omega_s}{\Delta t}, \quad (39)$$

where the superscript (k) is used to indicate the current time level. Using the middle

point rule, expressions (38) and (39) further reduce to

$$\frac{\partial}{\partial t} \int_{\Omega_s} T d\Omega_s = \frac{A}{\Delta t} (T^{(k)} - T^{(k-1)}), \tag{40}$$

$$\frac{\partial}{\partial t} \int_{\Omega_s} \omega d\Omega_s = \frac{A}{\Delta t} (\omega^{(k)} - \omega^{(k-1)}), \tag{41}$$

where A is the area of Ω_s .

We calculate the convection terms in the form

$$\int_{\Omega_s} \left(\frac{\partial(uT)}{\partial x} + \frac{\partial(vT)}{\partial y} \right) d\Omega_s = \int_{x_w}^{x_e} (vT) \Big|_n dx - \int_{x_w}^{x_e} (vT) \Big|_s dx + \int_{y_s}^{y_n} (uT) \Big|_e dy - \int_{y_s}^{y_n} (uT) \Big|_w dy, \tag{42}$$

$$\int_{\Omega_s} \left(\frac{\partial(u\omega)}{\partial x} + \frac{\partial(v\omega)}{\partial y} - \frac{\partial(T)}{\partial x} \right) d\Omega_s = \int_{x_w}^{x_e} (v\omega) \Big|_n dx - \int_{x_w}^{x_e} (v\omega) \Big|_s dx + \int_{y_s}^{y_n} (u\omega - T) \Big|_e dy - \int_{y_s}^{y_n} (u\omega - T) \Big|_w dy, \tag{43}$$

and treat the diffusion terms in the same way as for Poisson equation in Section 3.2.1.

Boundary conditions for the vorticity equation (34) are not given explicitly. One can compute them through equation (33) using given derivative boundary conditions for the streamfunction. In the case of rectangular boundaries, values of $\partial\psi/\partial n$ are incorporated into the computational boundary conditions for ω by means of the integration constants [Mai-Duy (2005); Mai-Duy and Tanner (2005)]. In the case of irregular boundaries, we apply the equations reported in [Le-Cao, Mai-Duy, and Tran-Cong (2009)]

$$\omega_b = - \left[1 + \left(\frac{t_x}{t_y} \right)^2 \right] \frac{\partial^2 \psi_b}{\partial x^2} - q_y, \tag{44}$$

$$\omega_b = - \left[1 + \left(\frac{t_y}{t_x} \right)^2 \right] \frac{\partial^2 \psi_b}{\partial y^2} - q_x, \tag{45}$$

where $t_x = \partial x / \partial s$, $t_y = \partial y / \partial s$, s is the tangential direction of boundary, and q_x, q_y are the known quantities defined as

$$q_x = -\frac{t_y}{t_x^2} \frac{\partial^2 \psi_b}{\partial y \partial s} + \frac{1}{t_x} \frac{\partial^2 \psi_b}{\partial x \partial s}, \quad (46)$$

$$q_y = -\frac{t_x}{t_y^2} \frac{\partial^2 \psi_b}{\partial x \partial s} + \frac{1}{t_y} \frac{\partial^2 \psi_b}{\partial y \partial s}. \quad (47)$$

The solution procedure involves the following steps

1. Solve equation (36) for ψ , subject to Dirichlet conditions
2. Compute the velocity components u and v , and the boundary values for the vorticity ω
3. Solve equation (35) for T , subject to Dirichlet and Neumann boundary conditions for natural convection in a square slot (Example 4.4.1), and to Dirichlet boundary conditions for natural convection in an annulus (Example 4.4.2)
4. Solve equation (37) for ω , subject to Dirichlet conditions
5. Repeat the above steps until the solution has reached the steady state.

4 Numerical examples

The proposed CLIRBF-FVM is verified in a series of 1D and 2D problems. If the exact solution is available, the accuracy of the approximate solution is measured using the relative discrete L_2 norm

$$Ne(u) = \frac{\sqrt{\sum_{i=1}^n (u_i - u_i^e)^2}}{\sqrt{\sum_{i=1}^n (u_i^e)^2}}, \quad (48)$$

where n is the number of collocation nodes, and u_i and u_i^e are the computed and exact solutions, respectively. We simply choose the MQ width as $a_i = \beta h$, where β is a given number, and h is a grid spacing. Results by the standard FVM [Patankar (1980)] and the point-collocation method employed with compact local IRBF stencils (CLIRBF-PCM) [Mai-Duy and Tran-Cong (2011)] are also included to provide the base for the assessment of the performance of the present method.

4.1 Example 1 (1D problem)

Consider the following ODE

$$\frac{\partial^2 u}{\partial x^2} + \frac{\partial u}{\partial x} + u = -\exp(-5x) [9979 \sin(100x) + 900 \cos(100)], \quad 0 \leq x \leq 1. \quad (49)$$

The exact solution to this problem is taken as $u^e(x) = \exp(-5x) \sin(100x)$. We discretise the domain using $\{71, 73, \dots, 591\}$ uniformly distributed nodes. The solution accuracy and the matrix condition number versus the grid size are shown in Figure 4 for Dirichlet boundary conditions only and in Figure 5 for Dirichlet and Neumann boundary conditions.

It can be seen that the proposed CLIRBF-FVM (1 Gauss point) outperforms the standard FVM, and the proposed CLIRBF-FVM (3 Gauss point) outperforms CLIRBF-PCM regarding both the solution accuracy and convergence rate. High rates of convergence are obtained with CLIRBF-FVM employed with the 3-point Gaussian quadrature rule as expected. The control-volume formulation is much more accurate than the point-collocation formulation, especially for the case of Neumann boundary conditions. Regarding the numerical stability, the condition numbers of the system matrix by the present method are similar to those by the standard FVM and CLIRBF-PCM for the case of Dirichlet boundary conditions only, but much lower than those by CLIRBF-PCM for the case of Dirichlet and Neumann boundary conditions.

4.2 Example 2 (2D problem, rectangular domain)

We take the following Poisson equation to verify the present method

$$\frac{\partial^2 u}{\partial x^2} + \frac{\partial^2 u}{\partial y^2} = 4(1 - \pi^2) \sin(2\pi x) \sinh(2y) + 16(1 - \pi^2) \cosh(4x) \cos(4\pi y), \quad (50)$$

where $-0.5 \leq x, y \leq 0.5$. Its exact solution is given by $u^e(x, y) = \sin(2\pi x) \sinh(2y) + \cosh(4x) \cos(4\pi y)$. The calculation is carried out with several grid densities $\{7 \times 7, 9 \times 9, \dots, 71 \times 71\}$. The solution accuracy and condition number by CLIRBF-FVM and CLIRBF-PCM are shown in Figures 6 and 7. The former is for Dirichlet boundary conditions, while the latter is for Dirichlet and Neumann boundary conditions, where u is specified on the left and right boundaries ($x = -0.5$ and $x = 0.5$) and $\partial u / \partial x$ is prescribed on the bottom and top boundaries ($y = -0.5$ and $y = 0.5$). Remarks here are similar to the 1D problems, using the middle-point rule is able to lead to a solution $O(h^2)$, while the 3-point Gaussian quadrature rule results in a solution with a very high rate of convergence, up to $O(h^{5.03})$.

Figure 8 shows the influence of the MQ width measured via β on the solution accuracy, which is investigated on three grids $\{31 \times 31, 41 \times 41, 51 \times 51\}$. It can

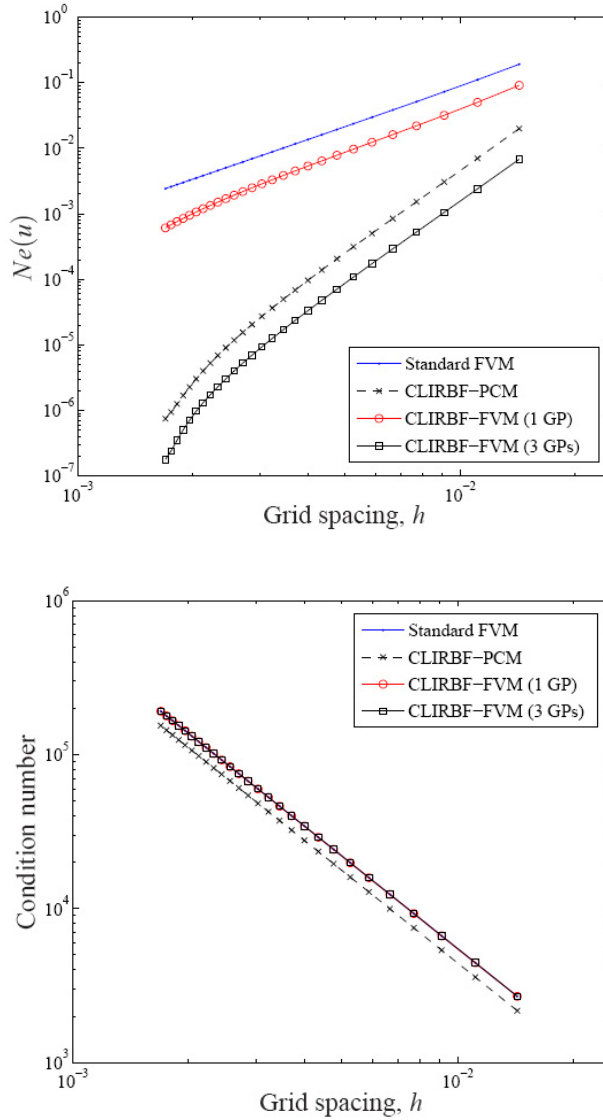


Figure 4: Example 1, ODE, Dirichlet boundary conditions: Relative L_2 errors of the solution u (top) and condition numbers of the system matrix (bottom) against the grid size by the standard FVM, CLIRBF-PCM, CLIRBF-FVM (1 Gauss point) and CLIRBF-FVM (3 Gauss points). Their behaviours are, respectively, $O(h^{2.03})$, $O(h^{4.72})$, $O(h^{2.30})$ and $O(h^{4.81})$ for the solution accuracy, and $O(h^{2.00})$, $O(h^{2.00})$, $O(h^{2.00})$ and $O(h^{2.00})$ for the matrix condition number.

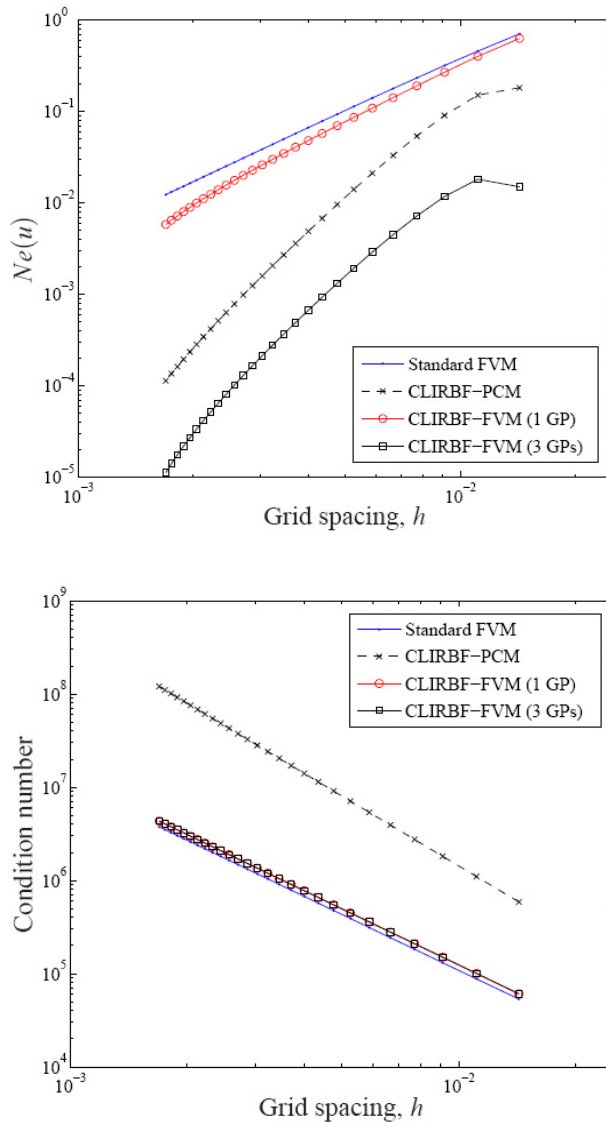


Figure 5: Example 1, ODE, Dirichlet and Neumann boundary conditions: Relative L_2 errors of the solution u (top) and condition numbers of the system matrix (bottom) against the grid size by the standard FVM, CLIRBF-PCM, CLIRBF-FVM (1 Gauss point) and CLIRBF-FVM (3 Gauss points). Their behaviours are, respectively, $O(h^{1.93})$, $O(h^{3.83})$, $O(h^{2.22})$ and $O(h^{3.88})$ for the solution accuracy, and $O(h^{2.00})$, $O(h^{2.50})$, $O(h^{2.00})$ and $O(h^{2.00})$ for the matrix condition number.

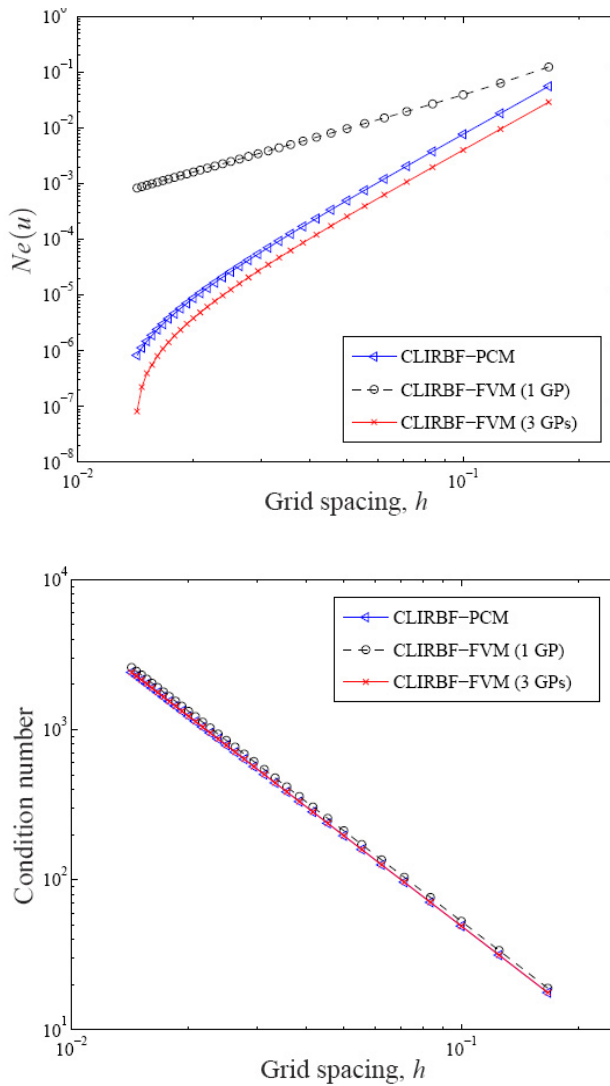


Figure 6: Example 2, PDE, rectangular domain, Dirichlet boundary condition: Relative L_2 errors of the solution u (top) and condition numbers of the system matrix (bottom) against the grid size by the CLIRBF-PCM, CLIRBF-FVM (1 Gauss point) and CLIRBF-FVM (3 Gauss points). Their behaviours are, respectively, $O(h^{4.42})$, $O(h^{2.00})$ and $O(h^{4.72})$ for the solution accuracy, and $O(h^{2.00})$, $O(h^{2.00})$ and $O(h^{2.00})$ for the matrix condition number.

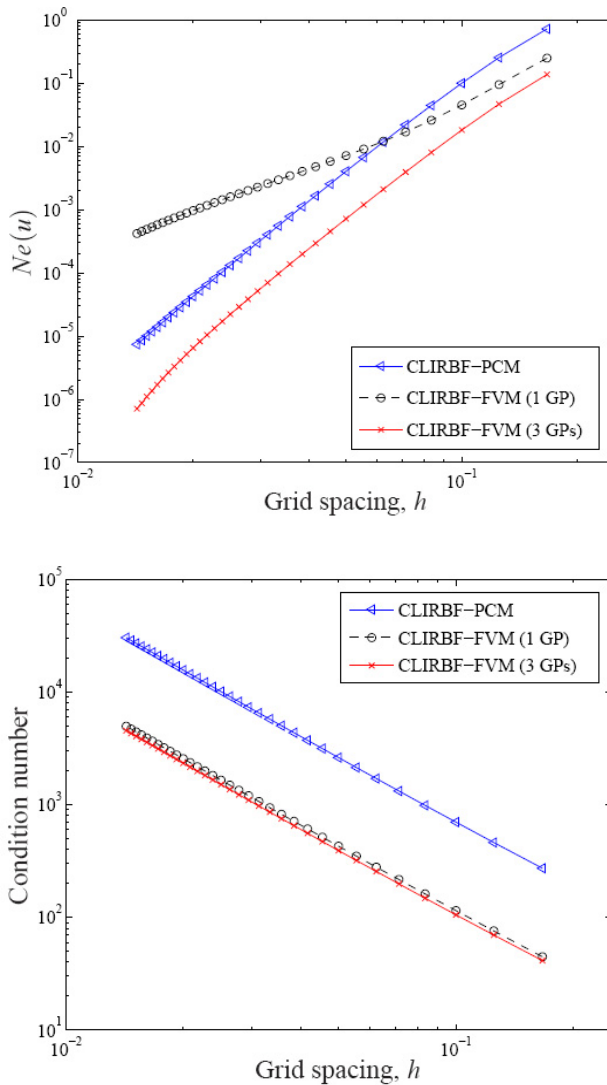


Figure 7: Example 2, PDE, rectangular domain, Dirichlet and Neumann boundary conditions: Relative L_2 errors of the solution u (top) and condition numbers of the system matrix (bottom) against the grid size by the CLIRBF-PCM, CLIRBF-FVM (1 Gauss point) and CLIRBF-FVM (3 Gauss points). Their behaviours are, respectively, $O(h^{4.82})$, $O(h^{2.42})$ and $O(h^{5.03})$ for the solution accuracy, and $O(h^{1.93})$, $O(h^{1.93})$ for the matrix condition number.

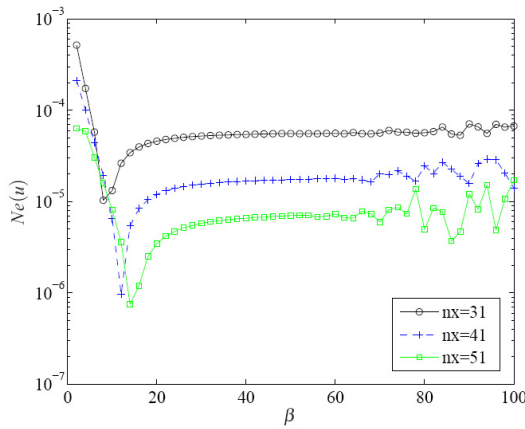


Figure 8: Example 2, PDE, rectangular domain, $\{31 \times 31, 41 \times 41, 51 \times 51\}$: the effect of the MQ width on the solution accuracy.

be seen that the present scheme can work well for a wide range of β . However, the optimal value of β and its stable range (e.g. 20 to 60 in this particular example) are problem-dependent. Generally, one needs to choose small values of β when the solution involves steep gradients.

4.3 Example 3 (2D problem, non-rectangular domain)

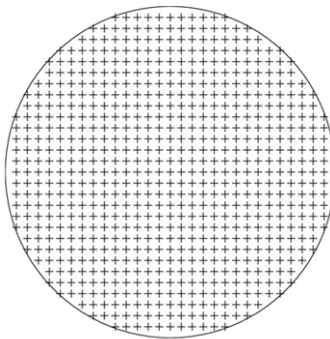


Figure 9: Non-rectangular domain: circular domain and its discretisation

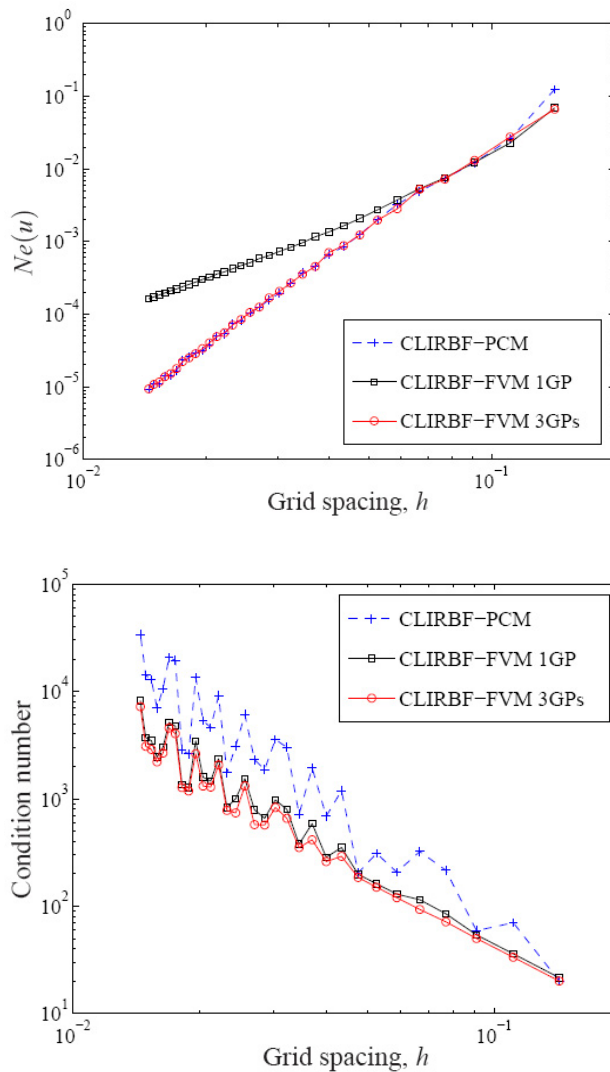


Figure 10: Example 3, PDE, non-rectangular domain, Dirichlet boundary condition: Relative L_2 errors of the solution u and condition numbers of the system matrix against the grid size by the CLIRBF-PCM, CLIRBF-FVM (1 Gauss point) and CLIRBF-FVM (3 Gauss points). Their behaviours are, respectively, $O(h^{4.03})$, $O(h^{2.44})$ and $O(h^{3.98})$ for the solution accuracy, and $O(h^{2.85})$, $O(h^{2.39})$ and $O(h^{2.37})$ for the matrix condition number.

Consider the same PDE as in Example 2. However, the domain of interest is of circular shape of radius $1/2$ and the boundary conditions are of Dirichlet type. Results obtained are presented in Figure 10. It shows that the numerical solution converges fast - apparently as $O(h^4)$ - for both CLIRBF-PCM and CLIRBF-FVM (3 Gauss points), and CLIRBF-FVM is more stable than CLIRBF-PCM. It also shows that the 1-point Gaussian quadrature scheme results in larger error than 3-point scheme. The error of the former is of order h^2 only at fine grids.

4.4 Example 4: Thermally-Driven Cavity Flow Problem

4.4.1 Natural convection in square slot

Consider a flow in a stationary unit square cavity ($0 \leq x, y \leq 1$), where the two side walls are heated with $T = 1$ at $x = 0$ and $T = 0$ at $x = 1$, while the top and the bottom walls are insulated ($\partial T / \partial y = 0$ at $y = 0$ and $y = 1$) (Figure 11). The no-slip boundary conditions lead to $\psi = 0$ and $\partial \psi / \partial n = 0$ on the four walls.

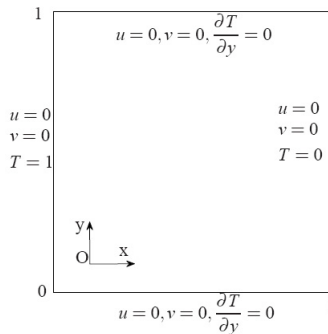


Figure 11: Geometry and boundary conditions for natural convection in a square slot.

Some important measures associated with this type of flow are

- Maximum horizontal velocity u_{max} on the vertical mid-plane and its location
- Maximum vertical velocity v_{max} on the horizontal mid-plane and its location
- The average Nusselt number throughout the cavity, which is defined as

$$\overline{Nu} = \int_0^1 Nu(x) dx, \tag{51}$$

$$Nu(x) = \int_0^1 \left(uT - \frac{\partial T}{\partial x} \right) dy, \tag{52}$$

Table 1: Natural convection in a square slot: Maximum velocities on the middle planes and the average Nusselt number by the present CLIRBF-FVM (3 Gauss points) and by some other methods.

Ra	Density	u_{max}	x	v_{max}	y	\overline{Nu}	$Nu_{1/2}$	Nu_0
10^3	11×11	3.612	0.814	3.693	0.177	1.121	1.117	1.120
	21×21	3.648	0.813	3.698	0.179	1.118	1.118	1.117
	GRBF ^a	-	-	-	-	1.118	1.119	1.117
	LBM ^b	3.648	0.810	3.697	0.180	1.116	-	-
	FDM ^c	3.649	0.813	3.697	0.178	1.118	1.118	1.117
10^4	31×31	16.059	0.823	19.612	0.118	2.247	2.240	2.246
	41×41	16.164	0.823	19.643	0.119	2.247	2.245	2.247
	GRBF ^a	-	-	-	-	2.247	2.248	2.244
	LBM ^b	16.138	0.820	19.602	0.120	2.230	-	-
	FDM ^c	16.178	0.823	19.617	0.119	2.243	2.243	2.238
10^5	41×41	34.61	0.854	68.98	0.065	4.535	4.530	4.527
	51×51	34.73	0.855	68.93	0.066	4.527	4.526	4.509
	GRBF ^a	-	-	-	-	4.529	4.530	4.521
	LBM ^b	34.459	0.855	68.551	0.065	4.488	-	-
	FDM ^c	34.73	0.855	68.59	0.066	4.519	4.519	4.509
10^6	61×61	64.44	0.851	222.73	0.0372	8.833	8.821	8.809
	71×71	64.59	0.850	222.12	0.0375	8.849	8.840	8.840
	GRBF ^a	-	-	-	-	8.864	8.865	8.827
	LBM ^b	63.413	0.848	219.708	0.036	8.745	-	-
	FDM ^c	64.63	0.8507	219.36	0.0379	8.800	8.799	8.817
	SM ^d	64.83	0.850	220.6	0.038	8.825	8.825	-
10^7	91×91	155.057	0.864	749.835	0.021	16.555	16.536	16.815
	GRBF ^a	-	-	-	-	16.661	16.661	-
	SM ^d	148.595	0.879	699.179	0.021	16.523	16.523	-

^a Galerkin-RBF method [Ho-Minh, Mai-Duy, and Tran-Cong (2009)]

^b Thermal BGK lattice Boltzmann model [Hao-Chueh, Kuen-Hau, Cheng-Hsiu, and Chao-An (2010)]

^c Finite difference method [Davis (1983)]

^d Spectral method [Quere (1991)]

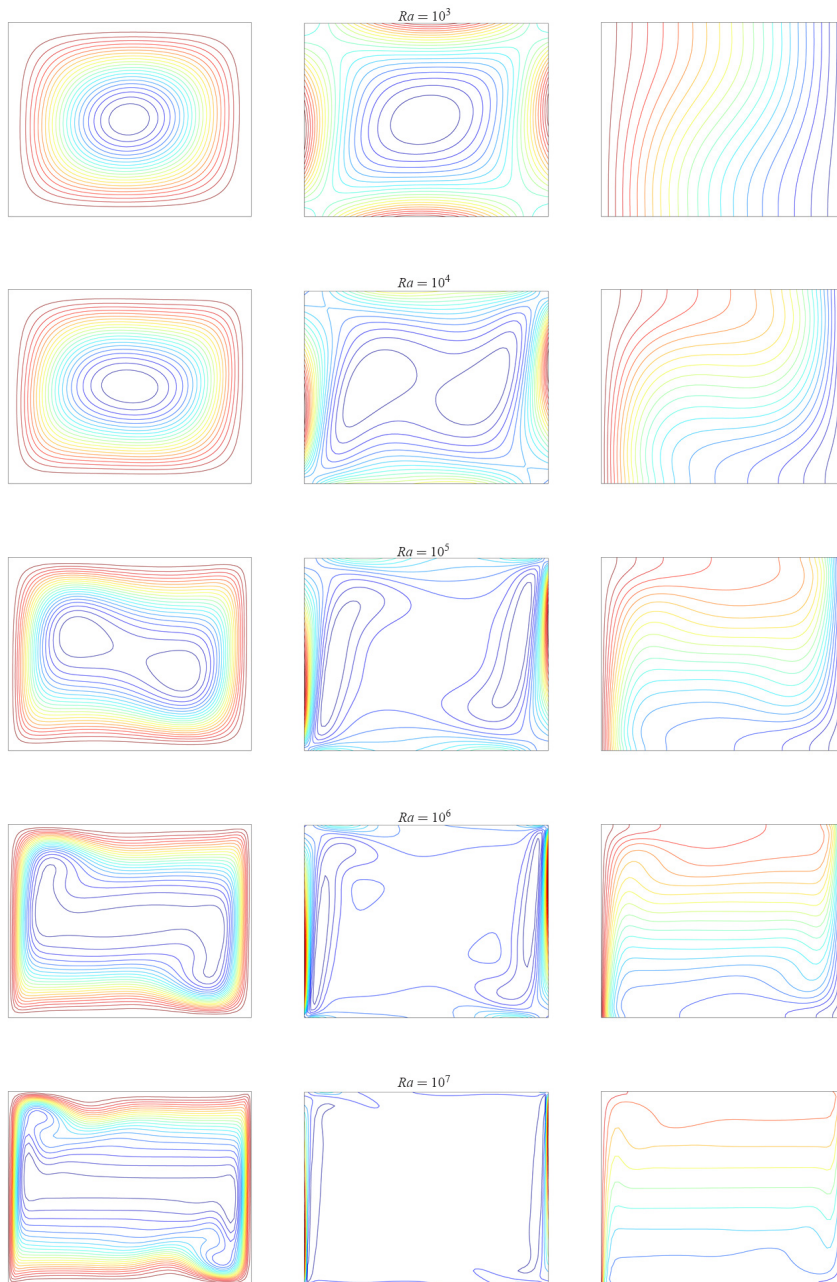


Figure 12: Natural convection in a square slot, 71×71 : Contour plots for the streamfunction (left), vorticity (middle), and temperature (right) for several Ra numbers.

in which $(uT - \partial T/\partial x)$ is the local heat flux in the horizontal direction

- The average Nusselt number on the vertical plane at $x = 0$ (left wall) and at $x = 1/2$ (middle cross-section), which are defined by

$$Nu_0 = Nu(x = 0, y)$$

$$Nu_{1/2} = Nu(x = 1/2, y)$$

A wide range of Ra , ($10^3, 10^4, \dots, 10^7$), and $Pr = 0.71$ are considered. The initial solution is taken from the computed solution at the lower and nearest value of Ra . For $Ra = 10^3$, the simulation starts with the fluid at rest.

Table 1 shows results obtained by the present method using the 3-point Gaussian quadrature rule, the benchmark solutions provided by G. De Vahl Davis [Davis (1983)] for $10^3 \leq Ra \leq 10^6$, and by P. Le Quere [Quere (1991)] for $Ra \geq 10^6$, and some other numerical results. It can be seen that (i) very good agreement is achieved between these results; and (ii) the present solutions are in better agreement with the benchmark ones than those obtained by the Galerkin-RBF approach [Ho-Minh, Mai-Duy, and Tran-Cong (2009)], and the thermal BGK lattice Boltzmann [Hao-Chueh, Kuen-Hau, Cheng-Hsiu, and Chao-An (2010)]. Figure 12 displays the distribution of the streamfunction, vorticity and temperature over the flow domain. They look feasible in comparison with those reported in the literature.

4.4.2 Natural convection in a concentric annulus between an outer square cylinder and an inner circular cylinder

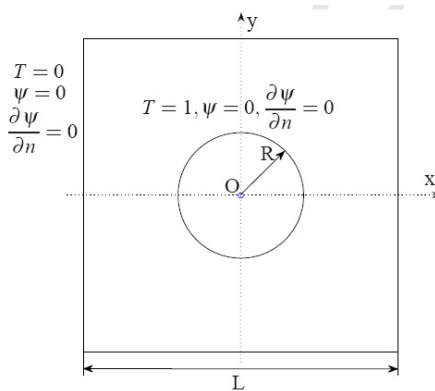


Figure 13: Geometry and boundary conditions for natural convection in a concentric annulus between an outer square cylinder and an inner circular cylinder.

Table 2: Natural convection in an annulus defined by concentric outer square and inner circular cylinders: the average Nusselt number on the outer (Nu_o) and inner (Nu_i) cylinders by the present CLIRBF-FVM (1 Gauss point) and by some other methods (RBF, FVM and DQM).

Ra	10^4	5×10^4	10^5	5×10^5	10^6
Grid	Nu_o				
32×32	3.22	3.98	4.78	7.30	8.67
42×42	3.22	4.01	4.83	7.38	8.63
52×52	3.22	4.04	4.88	7.52	8.77
62×62	3.22	4.04	4.88	7.51	8.93
1D-IRBF ^a	3.22	4.04	4.89	7.43	8.70
LMLS-IRBF ^b	3.23	4.05	4.91	7.43	8.67
FVM ^c	3.24		4.86		8.90
DQM ^d	3.33		5.08		9.37
Grid	Nu_i				
32×32	3.21	3.97	4.77	7.49	8.89
42×42	3.21	4.00	4.83	7.45	8.78
52×52	3.22	4.02	4.86	7.55	8.98
62×62	3.22	4.03	4.88	7.51	8.90
1D-IRBF ^a	3.21	4.04	4.89	7.51	8.85
LMLS-IRBF ^b	3.23	4.06	4.92	7.55	8.90
FVM ^c	3.24		4.86		8.90
DQM ^d	3.33		5.08		9.37

^a One dimensional integrated-RBF [Le-Cao, Mai-Duy, and Tran-Cong (2009)]

^b Local moving least square - one-dimensional IRBF [Ngo-Cong, Mai-Duy, Karunasena, and Tran-Cong (2012)]

^c Finite volume method [Moukalled and Acharya (1996)]

^d Differential quadrature method [Shu and Zhu (2002)]

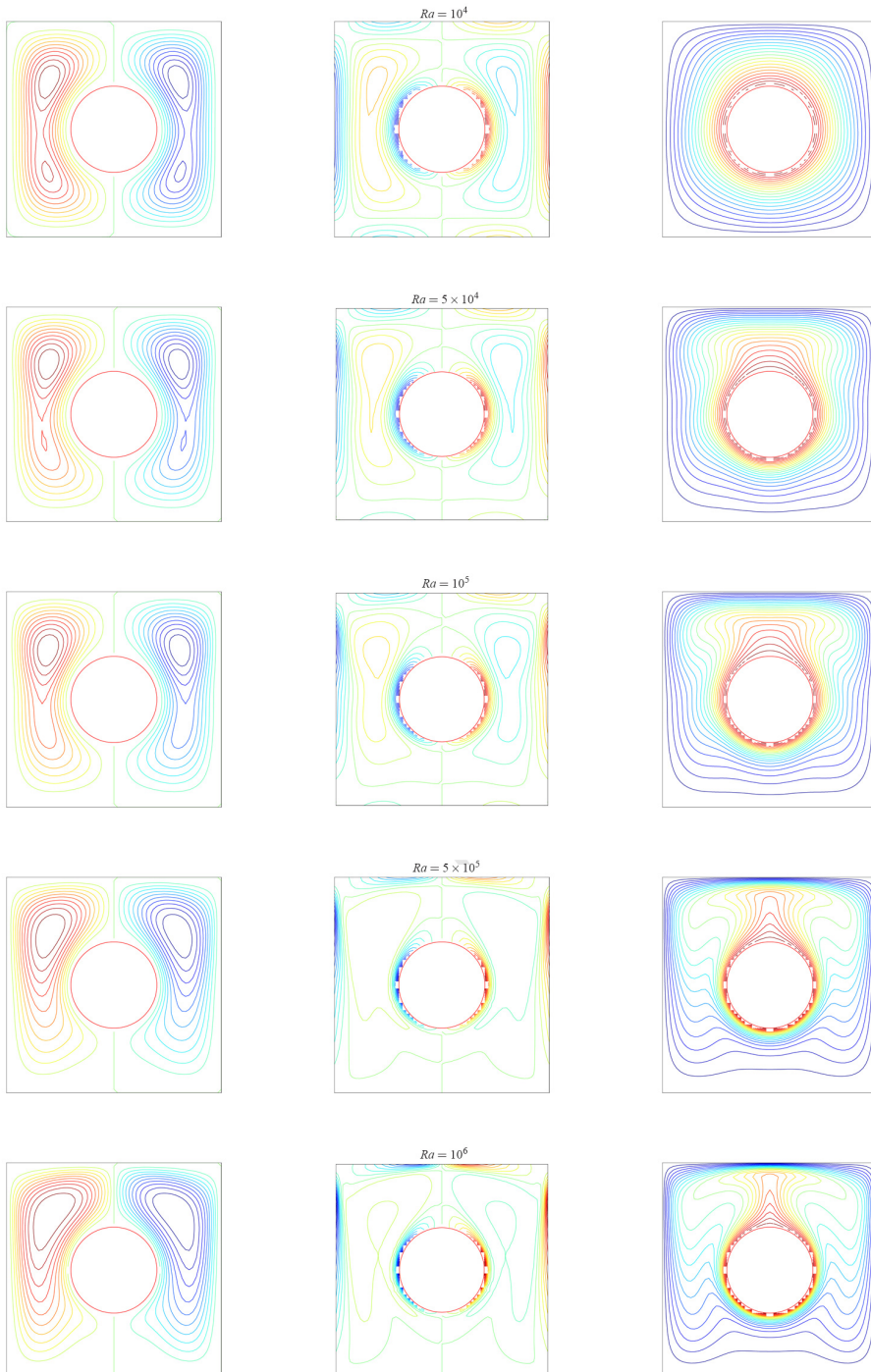


Figure 14: Natural convection in a concentric annulus between an outer square cylinder and an inner circular cylinder, 62×62 : Contour plots for the streamfunction (left), vorticity (middle), and temperature (right) for several Ra numbers.

The geometry and boundary condition of the problem are displayed in Figure 13. We take the ratio between the radius R of the inner cylinder and the side length L of the outer square to be 0.2. The Prandtl number is fixed at 0.71 and the Rayleigh number is varied in a range of $(10^4, 5 \times 10^4, 10^5, 5 \times 10^5, 10^6)$. The average Nusselt number is defined by

$$Nu = -\frac{1}{k} \oint \frac{\partial T}{\partial n} ds, \quad (53)$$

where k is the thermal conductivity.

Results concerning the average Nusselt number at the outer walls Nu_o and at the inner walls Nu_i are presented in Table 2. They agree well with other results ([Le-Cao, Mai-Duy, and Tran-Cong (2009); Moukalled and Acharya (1996); Shu and Zhu (2002); Ngo-Cong, Mai-Duy, Karunasena, and Tran-Cong (2012)]).

Figure 14 shows the contours of the streamfunction, vorticity, and temperature of the flow for several values of the Rayleigh number. At $Ra = 10^4$, their distributions are nearly symmetric about the horizontal axis across the cylinder centre. These distributions become more unsymmetric with increasing Ra (higher convection strength).

5 Concluding remarks

This paper presents a new finite-volume method for the simulation of heat transfer and fluid flow problems on rectangular and nonrectangular domains. The use of compact local IRBF approximations instead of the usual linear interpolations to represent the field variable and the employment of high-order integration schemes rather than the middle-point rule can lead to a significant improvement in accuracy for a finite-volume solution. The method is verified in analytic test problems for which high rates of convergence of the solution are achieved and in natural convection flows for which a convergent and accurate solution at high Ra number is obtained.

Acknowledgement

The first author would like to thank CESRC, FoES and USQ for a PhD scholarship. This research was supported by the Australian Research Council.

References

- Davis, G.** (1983): Natural convection of air in a square cavity: a benchmark numerical solution. *International Journal for Numerical Methods in Fluids*, vol. 3, pp. 249–264.

Epperson, J. (2002): *An introduction to numerical methods and analysis*. John Wiley, New York.

Eymard, R.; Gallouet, T.; Herbin, R. (2000): Finite volume methods: Schemes and analysis. *Handbook of numerical analysis*, vol. 7, pp. 713–1018.

Fasshauer, G. (2007): *Meshfree Approximation Methods With Matlab*. World Scientific Publishing, Singapore.

Fornberg, B.; Flyer, N. (2005): Accuracy of radial basis function interpolation and derivative approximations on 1-D infinite grids. *Advances in Computational Mathematics*, vol. 23, pp. 5–20.

Fornberg, B.; Wright, G. (2004): Stable computation of multiquadric interpolants for all values of the shape parameter. *Computers and Mathematics with Applications*, vol. 48, no. 5-6, pp. 853–867.

Hao-Chueh, M.; Kuen-Hau, L.; Cheng-Hsiu, Y.; Chao-An, L. (2010): A thermal lattice boltzmann model for flows with viscous heat dissipation. *Computer Modeling in Engineering and Sciences*, vol. 61, no. 1, pp. 45–63.

Haykin, S. (1999): *Neural Networks: A Comprehensive Foundation (second Edition)*, volume 842. Prentice Hall.

Ho-Minh, D.; Mai-Duy, N.; Tran-Cong, T. (2009): A Galerkin-RBF approach for the streamfunction-vorticity-temperature formulation of natural convection in 2D enclosed domains. *Computer Modeling in Engineering and Sciences*, vol. 44, no. 3, pp. 219–248.

Hoang-Trieu, T.-T.; Mai-Duy, N.; Tran-Cong, T. (2012): Several compact local stencils based on integrated RBFs for fourth-order ODEs and PDEs. *Computer Modeling in Engineering and Sciences*, vol. 84, no. 2, pp. 171–203.

Huilgol, R.; Phan-Thien, N. (1997): *Fluid Mechanics of Viscoelasticity*, volume 6. Elsevier Science Limited.

Kansa, E. (1990): Multiquadrics - A scattered data approximation scheme with applications to computational fluid-dynamics - I Surface approximations and partial derivative estimates. *Computers and Mathematics with Applications*, vol. 19, no. 8-9, pp. 127–145.

Kansa, E. (1990): Multiquadrics - A scattered data approximation scheme with applications to computational fluid-dynamics - II Solutions to parabolic, hyperbolic and elliptic partial differential equations. *Computers and Mathematics with Applications*, vol. 19, no. 8-9, pp. 147–161.

- Larsson, E.; Fornberg, B.** (2005): Theoretical and computational aspects of multivariate interpolation with increasingly flat radial basis functions. *Computers and Mathematics with Applications*, vol. 49, pp. 103–130.
- Le-Cao, K.; Mai-Duy, N.; Tran-Cong, T.** (2009): An effective intergrated-RBFN Cartesian-grid discretization for the streamfunction-vorticity-temperature formulation in nonrectangular domains. *Numerical Heat Transfer, Part B: Fundamentals*, vol. 55, no. 6, pp. 480–502.
- Lee, C. K.; Liu, X.; Fan, S. C.** (2003): Local multiquadric approximation for solving boundary value problems. *Computational Mechanics*, vol. 30, no. 5-6, pp. 396–409.
- Mai-Duy, N.** (2005): Solving high order ordinary differential equations with radial basis function networks. *International Journal for Numerical Methods in Engineering*, vol. 62, no. 6, pp. 824–852.
- Mai-Duy, N.; Tanner, R.** (2005): Solving high-order partial differential equations with indirect radial basis function networks. *International Journal for Numerical Methods in Engineering*, vol. 63, no. 11, pp. 1636–1654.
- Mai-Duy, N.; Tran-Cong, T.** (2001): Numerical solution of differential equations using multiquadric radial basis function networks. *Neural Networks*, vol. 14, pp. 185–199.
- Mai-Duy, N.; Tran-Cong, T.** (2001): Numerical solution of Navier-Stokes equations using multiquadric radial basis function networks. *International Journal for Numerical Methods in Fluids*, vol. 37, no. 1, pp. 65–86.
- Mai-Duy, N.; Tran-Cong, T.** (2009): A Cartesian-grid discretisation scheme based on local integrated RBFNs for two-dimensional elliptic problems. *Computer Modeling in Engineering and Sciences*, vol. 51, no. 3, pp. 213–238.
- Mai-Duy, N.; Tran-Cong, T.** (2011): Compact local integrated-RBF approximations for second-order elliptic differential problems. *Journal of Computational Physics*, vol. 230, no. 12, pp. 4772–4794.
- Moroney, T.; Turner, I.** (2006): A finite volume method based on radial basis functions for two-dimensional nonlinear diffusion equations. *Applied Mathematical Modelling*, vol. 30, pp. 1118–1133.
- Moukalled, F.; Acharya, S.** (1996): Natural convection in the annulus between concentric horizontal circular and square cylinders. *Journal of Thermophysics and Heat Transfer*, vol. 10, no. 3, pp. 524–531.
- Ngo-Cong, D.; Mai-Duy, N.; Karunasena, W.; Tran-Cong, T.** (2012): Local moving least square - one-dimensional IRBFN technique: Part I - natural convec-

tion flows in concentric and eccentric annuli. *Computer Modeling in Engineering and Sciences*, vol. 83, no. 3, pp. 275–310.

Patankar, S. (1980): *Numerical Heat Transfer and Fluid Flow*. Taylor and Francis Group.

Pereira, J.; Kobayashi, M.; Pereira, J. (2001): A fourth-order-accurate finite volume compact method for the incompressible Navier-Stokes solutions. *Journal of Computational Physics*, vol. 167, pp. 217–243.

Quere, P. (1991): Accurate solutions to the square thermally driven cavity at high Rayleigh number. *Computers Fluids*, vol. 20, no. 1, pp. 29–41.

Rippa, S. (1999): An algorithm for selecting a good value for the parameter c in radial basis function interpolation. *Advances in Computational Mathematics*, vol. 11, pp. 193–210.

Sarler, B. (2005): A radial basis function collocation approach in computational fluid dynamics. *Computer Modeling in Engineering and Sciences*, vol. 7, no. 2, pp. 185–193.

Shu, C.; Ding, H.; Yeo, K. (2003): Local radial basis function-based differential quadrature method and its application to solve two-dimensional incompressible Navier-Stokes equations. *Computer Methods in Applied Mechanics and Engineering*, vol. 192, pp. 941–954.

Shu, C.; Zhu, Y. (2002): Efficient computation of natural convection in a concentric annulus between an outer square cylinder and an inner circular cylinder. *International Journal for Numerical Methods in Fluids*, vol. 38, pp. 429–445.

Thai-Quang, N.; Le-Cao, K.; Mai-Duy, N.; Tran-Cong, T. (2012): A high-order compact local integrated-RBF scheme for steady-state incompressible viscous flows in the primitive variables. *Computer Modeling in Engineering and Sciences*, vol. 84, no. 6, pp. 528–557.

Tolstykh, A.; Shirobokov, D. (2005): Using radial basis functions in a “finite difference mode”. *Computer Modeling in Engineering and Sciences*, vol. 7, pp. 207–222.

Wright, G.; Fornberg, B. (2006): Scattered node compact finite difference-type formulas generated from radial basis functions. *Journal of Computational Physics*, vol. 212, no. 1, pp. 99–123.

Zerroukat, M.; Power, H.; Chen, C. (1998): A numerical method for heat transfer problems using collocation and radial basis functions. *International Journal for Numerical Methods in Engineering*, vol. 42, no. 7, pp. 1263–1278.